FRONTIERS OF PHYSICS

RESEARCH ARTICLE
Volume 22 / Issue 4 / 046201 / 2027

Prospects for precision YN and $\bar{n}N$ measurements with an LH_2/LD_2 target in the BESIII detector

Zhao-Ling Zhang[1], Xu Gao[1], Wei-Min Song[1,†], Chang-Zheng Yuan[2,3]

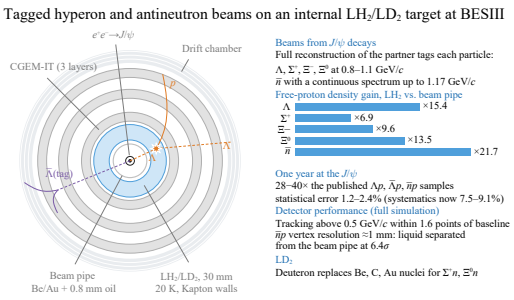
1 College of Physics, Jilin University, Changchun 130012, China
2 Institute of High Energy Physics, Chinese Academy of Sciences, Beijing 100049, China
3 University of Chinese Academy of Sciences, Beijing 100049, China
Corresponding author. E-mail: †weiminSong-JLU@jlu.edu.cn
Received August 7, 2026; accepted October 16, 2026

© Higher Education Press 2027

ABSTRACT

Tagged hyperon and antineutron beams from J/ψ and $\psi(3686)$ decays allow BESIII to study (anti)hyperon–nucleon (YN) and antineutron–nucleon ($\bar{n}N$) scattering, but the present measurements use the beam pipe as the target, whose only free protons are in a thin cooling-oil layer. We present a conceptual feasibility study of a liquid hydrogen (LH_2) or liquid deuterium (LD_2) target between the beam pipe and the Cylindrical Gas Electron Multiplier Inner Tracker. Relative to the beam pipe, a 30 mm LH_2 layer increases the effective free-proton areal density by factors of 7–22 for Λ, Σ^+, Ξ, and $\bar{n}$ beams (3.4 for Ω^-). A 30 mm LD_2 layer gives 0.9–2.9 times the effective neutron areal density for the same beams (0.4 for Ω^-) and replaces the composite Be, C, and Au nuclei with the deuteron. These ratios characterize the target itself and do not include channel-dependent efficiencies, backgrounds, or deuteron corrections. In detector simulations without localized support material, the target affects tracking mainly below 0.5 GeV/c; above this momentum, proton, kaon, and pion efficiencies stay within 1.6% of the baseline. In a signal-only full-event simulation of $\bar{n}p \to 2\pi^+\pi^-$, the LH_2-to-beam-pipe selection-efficiency ratio is 0.86, and the vertex and energy-closure resolutions are comparable to those for beam-pipe interactions. An internal LH_2/LD_2 target is thus a promising concept for higher-statistics and less model-dependent YN and $\bar{n}N$ measurements at BESIII, requiring further engineering and channel-level validation.

Keywords hyperon-nucleon scattering, antineutron-nucleon scattering, cryogenic internal target, effective luminosity, tracking performance, tau-charm factory



1 Introduction

Baryon–baryon and baryon–antibaryon interactions offer fundamental tests of the strong interaction in the nonperturbative regime of quantum chromodynamics (QCD) and provide critical insights into the internal structure of hadrons [1–6]. While scattering experiments provide the most direct probe of these forces, experimental progress has long been hindered by severe beam limitations: hyperons decay within a few centimeters, and antineutrons, being neutral, cannot be accelerated or cooled, so antineutron beams are available only as low-

https://doi.org/10.15302/frontphys.2027.046201

intensity secondary beams.

Hyperon–nucleon (YN) interactions generalize nuclear forces to the strangeness sector. Beyond probing $SU(3)$ flavor-symmetry breaking and dictating hypernuclear binding, they govern the properties of hyperonic matter inside neutron stars. Hyperons are predicted to appear in neutron-star cores at two to three times the nuclear saturation density, where they soften the equation of state (EOS) — a softening that generally conflicts with the astronomical observations of two-solar-mass pulsars [7–9]. Resolving this "hyperon puzzle", for instance via repulsive three-body YNN forces [10, 11], fundamentally requires high-precision constraints on the underlying two-body YN potentials. Historically, however, YN scattering data have been scarce, relying primarily on bubble-chamber measurements from the 1960s and 1970s [12–16]. Although recent experiments at J-PARC [17–19] and CLAS [20] have provided improved $\Sigma^{\pm}p$ and Λp data, the available kinematic coverage and statistical precision remain severely limited.

Consequently, modern YN potentials are calibrated primarily in the low-momentum regime. Chiral effective field theory (χEFT) potentials describe the coupled ΛN–ΣN system up to next-to-next-to-leading order [21], with covariant chiral formulations predicting cross sections up to ~ 900 MeV/c [22]. At higher momenta, existing CLAS Λp data between 0.9 and 2.0 GeV/c [20] already reveal substantial discrepancies, demonstrating the need for higher-order chiral potentials [22]. In this transition region, precise differential cross sections are essential, as they can break theoretical degeneracies among models that agree on total cross sections [22]. In the strangeness $S = -2$ sector, the ΞN interaction is even less constrained: lattice QCD near the physical point provides only low-energy S-wave predictions [23], and experimental data on channels such as $\Xi^0 n \to \Xi^- p$ have only emerged very recently.

In parallel, the nucleon–antinucleon ($\bar{N}N$) sector provides an indispensable laboratory for understanding annihilation dynamics and meson spectroscopy [24, 25]. In particular, the antineutron–proton ($\bar{n}p$) system represents a pure isospin $I = 1$ state completely free of the Coulomb interactions present in $\bar{p}p$ scattering. Past measurements, such as those at BNL E-767 [26] and OBELIX at CERN [27–29], used such beams produced via the charge-exchange reaction $\bar{p}p \to \bar{n}n$, and antineutron scattering data above 500 MeV/c remain scarce.

A breakthrough approach to overcome these beam limitations was proposed in Ref. [30]: utilizing charmonium (J/ψ and $\psi(3686)$) decays at high-luminosity e^+e^- colliders as a prolific source of tagged hyperons and antineutrons [31]. Due to large resonance production cross sections and sizable baryonic decay branching fractions, this method produces monoenergetic hyperon beams (such as Λ at 1074 MeV/c and Σ^+ at 992 MeV/c) as well as broad-spectrum antineutrons up to 1.17 GeV/c (Table 2). Fully reconstructing the recoiling partner baryon uniquely tags the incident projectile and determines its four-momentum from the two-body or three-body decay kinematics. BESIII has successfully demonstrated this concept by utilizing its existing beam pipe as an interaction target, producing pioneering measurements of $\bar{n}p$, $\Xi^0 n$, $\Lambda N \to \Sigma^+ X$, Λp, $\bar{\Lambda} p$, and $\Sigma^+ n$ processes [32–36].

Despite this success, beam-pipe scattering faces two intrinsic bottlenecks. First, free target protons exist only in the hydrogen atoms of a thin (0.8 mm) cooling-oil layer, which severely restricts the statistical precision and angular binning of differential cross-section measurements. Second, while the gold (Au) and beryllium (Be) layers and the carbon (C) of the cooling oil provide abundant nucleons, they are bound within nuclei; extracting fundamental, elementary baryon–nucleon cross sections from these targets requires substantial nuclear-model corrections, introducing irreducible systematic uncertainties.

Installing a dedicated, high-density cryogenic target can simultaneously resolve both limitations. While placing custom targets just outside the beam pipe was suggested in Ref. [30] and effective luminosities for existing detector materials were formulated in Ref. [31], this paper presents the first conceptual feasibility study of an internal liquid hydrogen (LH_2) or liquid deuterium (LD_2) target integrated directly into the BESIII detector. Located in the radial clearance between the beam pipe and the Cylindrical Gas Electron Multiplier Inner Tracker (CGEM-IT), an LH_2 target dramatically amplifies the free-proton areal density, while an LD_2 target replaces composite nuclear targets with the deuteron — providing a simple, weakly bound system for quasi-free neutron measurements.

The remainder of this paper is structured as follows. Section 2 details the target cell configuration, the passive material budget, and the kinematics of the incident hyperon and antineutron beams. Section 3 evaluates the impact of the added target material in the full BESIII Geant4 detector simulation, first on single charged tracks and then on the complete reconstruction of the exclusive channel $J/\psi \to p\pi^-\bar{n}$ with $\bar{n}p \to 2\pi^+\pi^-$. Section 4 quantifies the effective areal densities and presents projected annual signal yields and systematic uncertainty comparisons against existing beam-pipe measurements. Finally, Section 5 summarizes the findings and discusses the outlook for future facilities.

2 Target configuration and incident beams

2.1 Detector overview and target configuration

The BESIII detector [37] is a magnetic spectrometer at the BEPCII e^+e^- collider [38]. A multilayer drift chamber (MDC), a time-of-flight system (TOF), and a CsI(Tl) electromagnetic calorimeter (EMC) are enclosed in a

Table 1 Continuous passive-material layers of the nominal 30 mm target, in radial order, as included in the detector simulation of Section 3.

Component	Material and thickness
Inner vacuum window	Mylar–aramid laminate, 368 g/m^2 (simulated as 0.26 mm Mylar)
Inner MLI blanket	Al-Mylar, 10×0.006 mm
Inner target wall	Kapton, 0.1 mm
Liquid target	LH_2 or LD_2, 30 mm
Outer target wall	Kapton, 0.1 mm
Outer MLI blanket	Al-Mylar, 10×0.006 mm
Outer vacuum window	Mylar–aramid laminate, 368 g/m^2 (simulated as 0.26 mm Mylar)

superconducting solenoid that provides a 1.0 T magnetic field, and a muon chamber system (MUC) is embedded in the return yoke. The CGEM-IT replaces the inner part of the MDC [39].

The proposed target is an annular cryogenic cell in the radial gap between the outer surface of the beam pipe ($r = 33.7$ mm) and the inner radius of the CGEM-IT ($r = 76.9$ mm) [39]. In the nominal configuration, the liquid layer is 30 mm thick ($40.4 < r < 70.4$ mm) and extends over $|z| < 200$ mm, symmetric about the interaction point, so that it covers the full $|\cos\theta| < 0.8$ acceptance used in Section 4; together with its walls and insulation, it lies within $35 < r < 76$ mm.

The liquid is contained between inner and outer Kapton walls, each 0.1 mm thick. Kapton is a low-Z material ($Z_{\rm eff} \sim 5$) that tolerates radiation and remains mechanically robust at cryogenic temperatures. To limit radiative heat transfer, the cell is wrapped in a 10-layer aluminized-Mylar multi-layer insulation (MLI) blanket inside an evacuated insulation space closed by vacuum windows of Mylar laminated on aramid fabric. These materials are taken from the MUSE liquid-hydrogen target [40], which uses a 120 μm Kapton cell wall, 10 layers of aluminized-Mylar superinsulation, and 368 g/m^2 Mylar–aramid vacuum windows. Table 1 lists the layers in radial order, and Fig. 1 shows an r–z section of the target. As a candidate cooling scheme, an external Gifford–McMahon (GM) cryocooler would keep the liquid near its normal boiling point; its cold head and condenser would sit outside the main tracking acceptance, connected to the cell by a low-mass fill/return line.

At their normal boiling points of 20.3 and 23.7 K, liquid hydrogen and deuterium have densities of 0.0708 and 0.164 g·cm^{-3}. LH_2 provides free protons for Yp and $\bar{n}p$ scattering, so the signal interaction needs no bound-

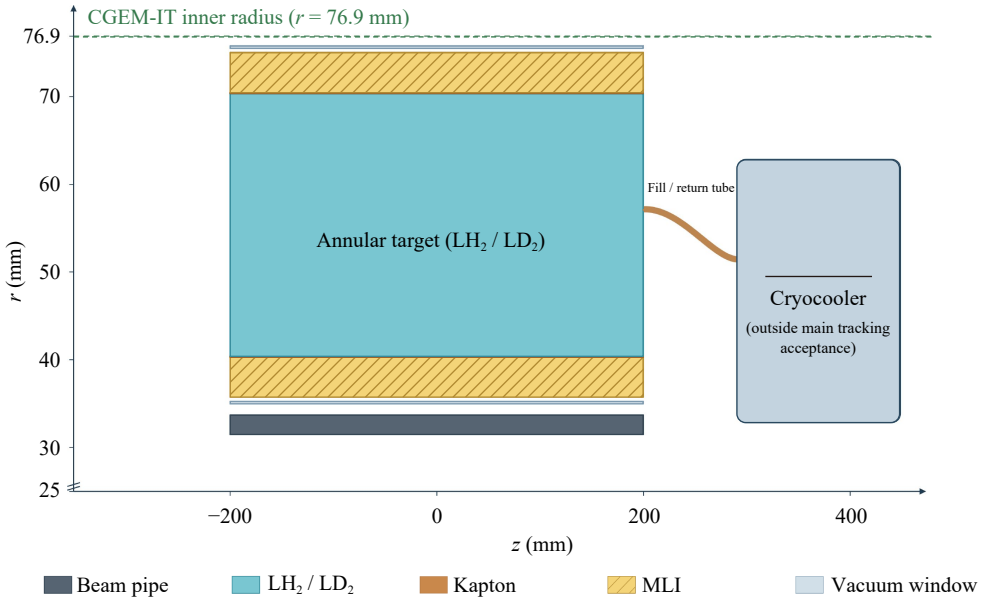


Fig. 1 Axial (r–z) schematic of the proposed BESIII cryogenic target. The annular LH_2/LD_2 volume between the beam pipe ($r = 33.7$ mm) and the CGEM-IT inner radius ($r = 76.9$ mm) is bounded by inner and outer Kapton walls and surrounded by multi-layer insulation and Mylar–aramid vacuum windows. A representative fill/return line and the external cryocooler are drawn schematically outside the main tracking acceptance.

Table 2 Production channels and inputs for the incident species. Branching fractions (BF), masses, and lifetimes are from PDG 2024 [48]; p is the momentum in the parent rest frame. The two errors on α are statistical and systematic; the Ω^- value has a combined error. The antineutron kinematics are taken from the PWA sample described in the text.

Species	Production	BF (10^{-3})	p (MeV/c)	m_Y (MeV/c^2)	τ_Y (10^{-10} s)	α
Λ	$J/\psi \to \Lambda\bar{\Lambda}$	1.89 ± 0.09	1074	1115.683 ± 0.006	2.617 ± 0.010	$0.4748 \pm 0.0022 \pm 0.0031$ [43]
Σ^+	$J/\psi \to \Sigma^+\bar{\Sigma}^-$	1.07 ± 0.04	992	1189.37 ± 0.07	0.8018 ± 0.0026	$-0.508 \pm 0.006 \pm 0.004$ [45]
Ξ^-	$J/\psi \to \Xi^-\bar{\Xi}^+$	0.97 ± 0.08	807	1321.71 ± 0.07	1.639 ± 0.015	$0.586 \pm 0.012 \pm 0.010$ [44]
Ξ^0	$J/\psi \to \Xi^0\bar{\Xi}^0$	1.17 ± 0.04	818	1314.86 ± 0.20	2.90 ± 0.09	$0.514 \pm 0.006 \pm 0.015$ [46]
Ω^-	$\psi(3686) \to \Omega^-\bar{\Omega}^+$	0.056 ± 0.003	774	1672.45 ± 0.29	0.821 ± 0.011	0.24 ± 0.10 [47]
$\bar{n}$	$J/\psi \to p\pi^-\bar{n}$	2.12 ± 0.09	0–1174	–	Stable	PWA sample

nucleon correction. LD_2 provides neutrons for Yn scattering with the crucial advantage of a much simpler and cleaner nuclear environment: each neutron is accompanied only by a single proton bound by 2.22 MeV, so that deuteron corrections, which can be treated as a few-body problem, replace the model-dependent treatment of the composite Be, C, and Au nuclei.

2.2 Incident beams and survival probabilities

The laboratory decay lengths $\lambda_Y = (p_Y/m_Y)\,c\tau_Y$ of the hyperons considered here, where p_Y, m_Y, and τ_Y are the momentum, mass, and lifetime, range from 1.1 cm for the Ω^- to 7.6 cm for the Λ, comparable to the radii of the target, so a sizable fraction decays before reaching the liquid or while crossing it. The flux reaching the target therefore depends on the momentum, lifetime, and angular distribution of each species, which we specify first.

The hyperons are produced in the two-body decays $J/\psi \to Y\bar{Y}$ for the Λ, Σ^+, and Ξ, and $\psi(3686) \to \Omega^-\bar{\Omega}^+$ for the Ω^-, whose pair production is kinematically forbidden in J/ψ decays. In the parent rest frame, each hyperon has a fixed momentum $p_Y = \sqrt{m^2_{\rm parent}/4 - m^2_Y}$ and the angular distribution $f_Y(\cos\theta) \propto 1 + \alpha\cos^2\theta$ [41, 42], normalized to unity over $-1 \le \cos\theta \le 1$, where α is the angular-distribution parameter of the production process measured by BESIII [43–47]. Table 2 lists these parameters together with the momenta, branching fractions, masses, and lifetimes [48]; the same inputs are used for the areal densities of Section 4.1. The small boost from the BEPCII beam-crossing angle is neglected for the hyperons. The angular acceptance $A_Y = \int_{-0.8}^{0.8} f_Y(\cos\theta)\,{\rm d}\cos\theta$, the fraction of produced particles with $|\cos\theta| < 0.8$, is 0.75–0.78 for the Λ, Ξ, and Ω^-, whose positive α favors production at small polar angles, and 0.859 for the Σ^+, whose negative $\alpha = -0.508$ favors production near 90°.

Antineutrons from the three-body decay $J/\psi \to p\pi^-\bar{n}$ have a continuous momentum spectrum up to 1.17 GeV/c, and their angular distribution cannot be described by a single $1 + \alpha\cos^2\theta$ form. We therefore use 5×10^5 events generated with the partial-wave-analysis (PWA) model of the BESIII measurement [32]. Of these events, 415 250 satisfy $|\cos\theta_{\bar{n}}| < 0.8$, giving $A_{\bar{n}} = 0.8305 \pm 0.0005$.

Following Ref. [31], a particle emitted at polar angle θ travels a path $r/\sin\theta$ to reach radius r and survives with probability

$$S_Y(r,\theta) = \exp\left(-\frac{r}{\lambda_Y \sin\theta}\right). \tag{1}$$

The accepted surviving fraction is its average over the accepted polar angles,

$$\frac{N(r)}{N_{\rm gen}} = \int_{-0.8}^{0.8} f_Y(\cos\theta)\, S_Y(r,\theta)\,{\rm d}\cos\theta, \tag{2}$$

where $N_{\rm gen}$ is the number of particles produced at the interaction point and $N(r)$ is the number that reach r within $|\cos\theta| < 0.8$; at $r = 0$ it equals A_Y. For the antineutron, $S_{\bar{n}} = 1$ and the fraction is the constant $A_{\bar{n}}$. Figure 2 shows the resulting curves.

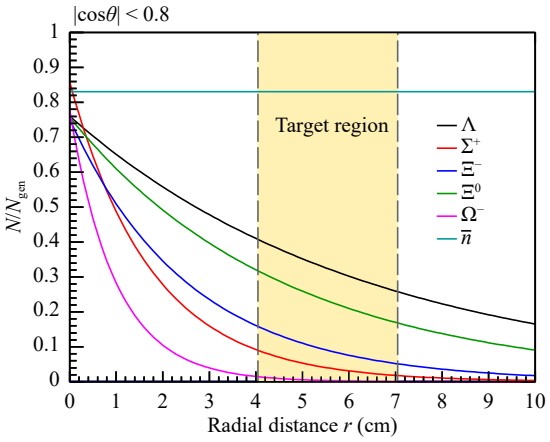


Fig. 2 Accepted surviving fraction $N/N_{\rm gen}$ of Λ, Σ^+, Ξ^-, Ξ^0, Ω^-, and $\bar{n}$ as a function of the radial distance r from the interaction point, computed from Eq. (1) averaged over $|\cos\theta| < 0.8$; the value at $r = 0$ equals the angular acceptance A_Y. The yellow band marks the target region. The antineutron line is the PWA acceptance $A_{\bar{n}} = 0.8305$.

3 Detector simulation and reconstruction performance

3.1 Simulation setup

The introduction of target material between the beam pipe and the CGEM-IT inevitably impacts charged-particle tracking via energy loss, multiple Coulomb scattering, and secondary hadronic interactions. Following the methodology in Ref. [49], we investigate these effects using the full BESIII detector simulation, systematically comparing the baseline detector (without target) against the nominal 30 mm LH_2 and LD_2 configurations, each incorporating the full passive material budget listed in Table 1. Localized mechanical supports, alignment spacers, and cryogenic service feedthroughs are omitted from the present model.

Both event simulation and track reconstruction are performed within the BESIII Offline Software System (BOSS), Version 7.2.0, utilizing the official geometry description with the CGEM-IT included [37, 39]. Particle transport is modeled with Geant4 (version 10.7.p02) using the `FTFP_BERT` physics list. BOSS 7.2.0 is a development release with preliminary CGEM-IT simulation and reconstruction, so absolute efficiencies and resolutions may differ from those of future production releases. We therefore compare each target configuration with the baseline using the same software version and simulation settings, and quote the changes relative to the baseline.

The performance evaluation relies on two complementary Monte Carlo samples: first, single-particle samples (p, $\bar{p}$, $K^{\pm}$, $\pi^{\pm}$) generated at the interaction point are used to assess basic tracking efficiencies and track parameter resolutions across all configurations (Section 3.2); second, a full-event exclusive sample of the reaction chain $J/\psi \to p\pi^-\bar{n}$ with $\bar{n}p \to 2\pi^+\pi^-$ is employed to benchmark complete multi-track vertexing and kinematic reconstruction for annihilations occurring in the beam pipe and in LH_2 (Section 3.3).

3.2 Single-particle tracking performance

The single-particle benchmark samples consist of protons, antiprotons, charged kaons, and charged pions generated at the nominal interaction point, with approximately 10^6 events simulated per species and target configuration, divided equally between the two charge states. Momentum and $\cos\theta$ are generated uniformly. The performance is compared in truth-momentum bins of 0.1 GeV/c over 0.3–1.5 GeV/c for protons and antiprotons, 0.2–1.5 GeV/c for kaons, and 0.1–1.5 GeV/c for pions, and in $|\cos\theta|$ bins of width 0.1. Each momentum projection integrates over the full angular acceptance, while each angular projection integrates over the accessible momentum range for that species.

A reconstructed track candidate is accepted if the Kalman-filter fit successfully converges under the mass hypothesis of the generated particle. A candidate is matched to the primary truth track if more than 50% of its associated MDC wire hits originate directly from that particle (excluding hits from secondary δ-electrons); hits associated with other particles or carrying ambiguous truth status count against the match. The reconstruction efficiency is defined as

$$\epsilon_{\rm rec} = \frac{N_{\rm match}}{N_{\rm gen}}, \tag{3}$$

where $N_{\rm match}$ denotes the number of generated particles with at least one matched candidate. If multiple candidates satisfy the matching criteria, the one possessing the greatest number of primary hits is chosen for evaluating track resolution.

Track parameter resolutions are evaluated via the relative momentum residual, $\delta_p = (p_{\rm rec} - p_{\rm truth})/p_{\rm truth}$, and the polar-angle residual, $\delta_\theta = \theta_{\rm rec} - \theta_{\rm truth}$. Their widths in each bin are determined from the unbinned distributions of matched tracks using the non-parametric estimator

$$\sigma_{68}(x) = \frac{q_{84.135}(x) - q_{15.865}(x)}{2}, \tag{4}$$

where q_a is the ath percentile of the residual distribution, so that σ_{68} is the half-width of its central 68.27% interval. The efficiency uncertainties are 68.27% Wilson score intervals for a binomial proportion [50], which remain within $[0, 1]$ and are reliable for efficiencies close to unity. The uncertainty of σ_{68} is estimated with the nonparametric bootstrap [51]: the matched tracks in each bin are resampled with replacement 2000 times, σ_{68} is recomputed for each resample, and the standard deviation of the 2000 values is quoted.

Figures 3–5 display the tracking performance across the baseline and target configurations. Target-induced degradation is predominantly confined to low momenta below 0.5 GeV/c (e.g., up to a 22 percentage-point reduction for protons in LD_2). Above 0.5 GeV/c, tracking efficiencies for protons, kaons, and pions remain robust, staying within 1.6 percentage points of the baseline. Antiprotons are an exception, showing a systematic deficit of up to 2.2 points in LH_2 and 4.9 points in LD_2; this loss scales directly with nucleon density and is governed by in-flight annihilation within the liquid target.

3.3 Full-event simulation of $\bar{n}p \to 2\pi^+\pi^-$

To evaluate full-event reconstruction, we simulate the complete reaction sequence $J/\psi \to p\pi^-\bar{n}$ followed by the annihilation $\bar{n}p \to 2\pi^+\pi^-$. The four-momenta of the tag proton, tag pion, and incident antineutron are sampled

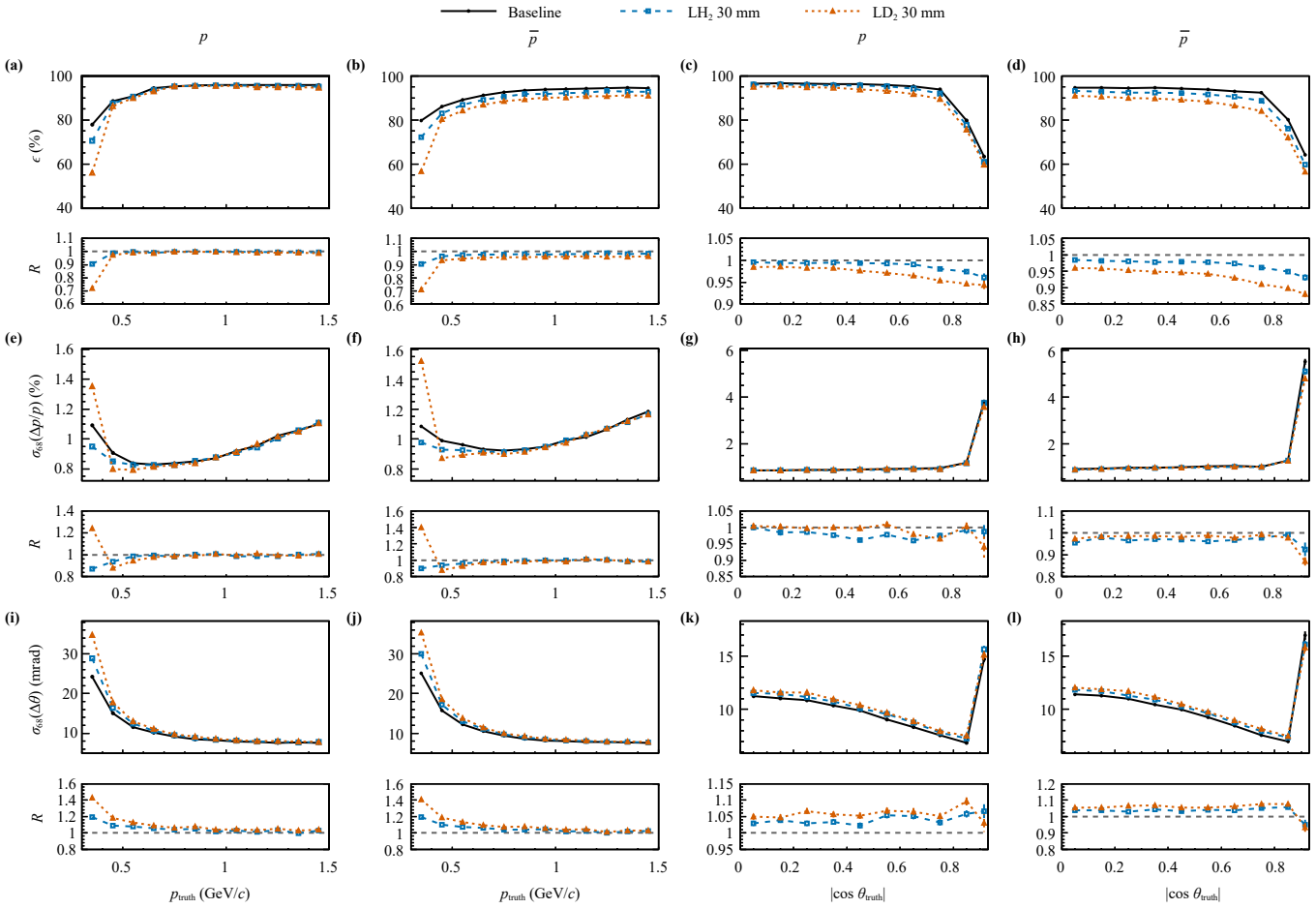


Fig. 3 Single-particle tracking performance for protons and antiprotons. Rows show the reconstruction efficiency, relative momentum-residual width $\sigma_{68}(\delta_p)$, and polar-angle width $\sigma_{68}(\delta_\theta)$. Columns show distributions versus truth momentum for protons and antiprotons, followed by distributions versus $|\cos\theta_{\rm truth}|$. Black circles, blue squares, and orange triangles represent the baseline, 30 mm LH_2, and 30 mm LD_2 setups, respectively. The sub-panel below each plot displays the ratio R of each target configuration to the baseline.

event-by-event using the PWA generator (Section 2.2), while the annihilation products follow three-body phase space on a stationary target proton. This yields 98 661 and 98 461 simulated events in the beam pipe and LH_2 target, respectively.

Charged-track candidates are required to have valid hits in the MDC, successfully converged Kalman-filter fits, and polar angles within the tracking acceptance $|\cos\theta| < 0.93$. The tag proton and negative pion must originate from the interaction region ($V_{xy} < 1.0$ cm, $|V_z| < 10.0$ cm) and are identified using combined $\mathrm{d}E/\mathrm{d}x$ and time-of-flight information. Each tag pair must pass a common vertex fit with $\chi^2 \leq 200$ and a one-constraint (1C) kinematic fit to the antineutron missing mass with $\chi^2 \leq 200$; if several pairs qualify, the one with the smallest sum of the two χ^2 values is kept, and its recoil mass, computed from the vertex-fitted momenta, must lie within $[0.89, 0.99]$ GeV/c^2. Upon removing the tag pair, exactly three remaining charged tracks with net charge $+1$ $(++-)$ are required. These three tracks are fitted to a common secondary vertex under the pion mass hypothesis, requiring $\chi^2 < 200$ and a transverse vertex radius $R_{xy} = \sqrt{x^2+y^2} \geq 10$ mm.

Of the simulated events, 26 938 in the beam pipe and 23 237 in LH_2 pass all requirements. The conditional selection efficiency $\epsilon_{\rm cond} = N_{\rm sel}/N_{\rm sim}$ is $(27.30 \pm 0.14)\%$ for the beam pipe and $(23.60 \pm 0.14)\%$ for LH_2, giving a ratio of 0.864 ± 0.007. About half of the loss occurs at the requirement of exactly three signal tracks (54.1% of tagged events for LH_2 versus 58.0% for the beam pipe), with smaller losses in the tag selection (67.6% versus 69.4%) and in the signal-pion track fits (77.8% versus 79.6%).

For resolution studies, we evaluate the transverse radial residual,

$$\Delta r = r_{\rm fit} - r_{\rm true}, \qquad r = \sqrt{x^2+y^2}, \tag{5}$$

where $r_{\rm true}$ is the transverse radius of the true annihilation vertex, and the energy closure,

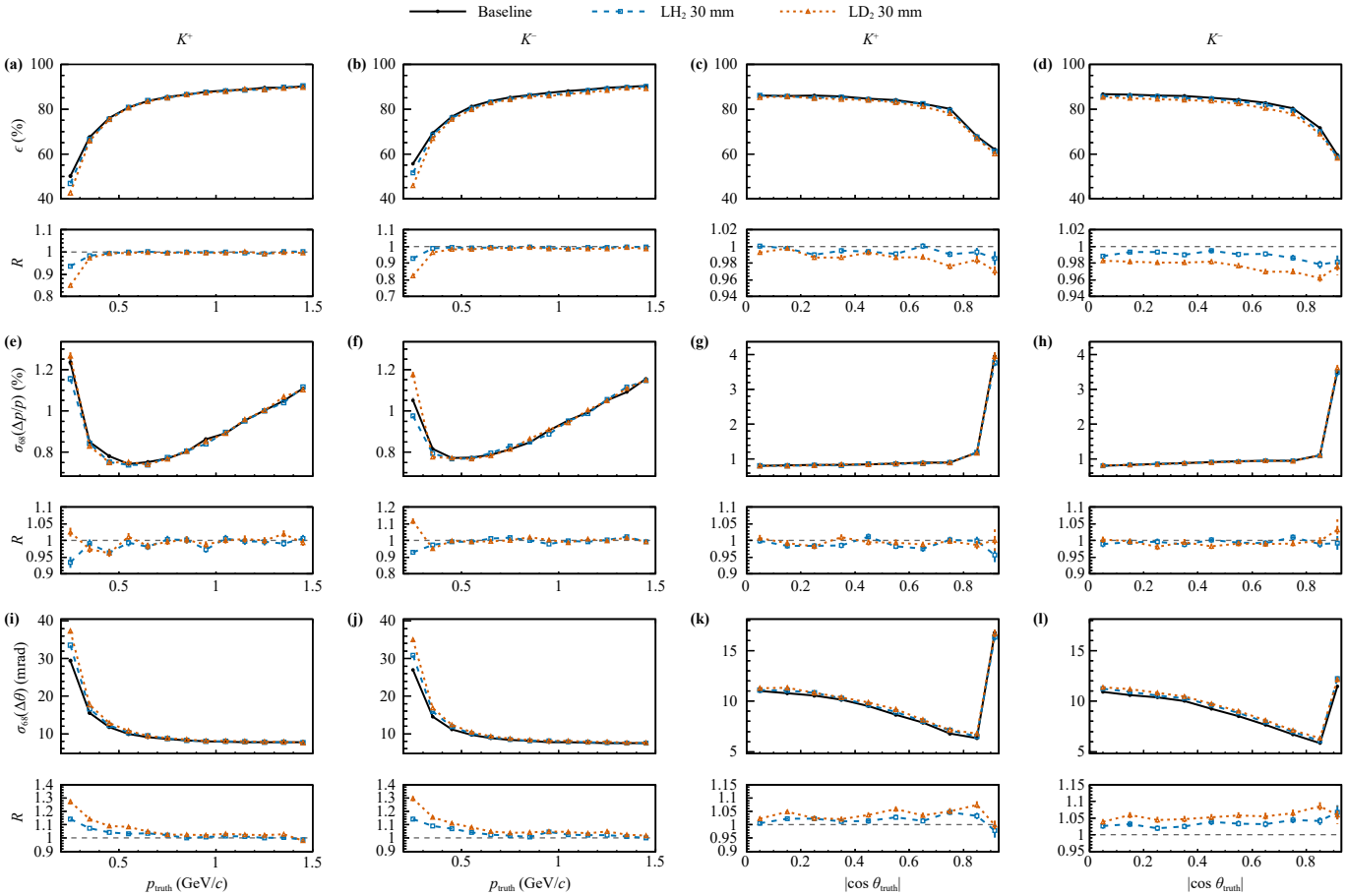


Fig. 4 Single-particle tracking performance for K^+ and K^-, using the same observables, layout, configurations, and axis conventions as in Fig. 3. The truth-momentum range spans 0.2–1.5 GeV/c.

$$\Delta E = \sum_{i=1}^{3} E_{\pi_i,\mathrm{VF}} - E_{\bar{n},\mathrm{tag\,1C}} - m_p, \tag{6}$$

here, the pion energies $E_{\pi_i,\mathrm{VF}}$ are taken from the common three-pion vertex fit, and the antineutron energy $E_{\bar{n},\mathrm{tag\,1C}}$ is obtained from the tag-side 1C fit.

Figure 6 compares the reconstructed distributions between the two target geometries. Resolution widths σ_{68} are calculated as half the difference between the 84th and 16th percentiles of each distribution, with statistical errors determined via 2000 bootstrap resamples. The beam-pipe and LH_2 configurations exhibit radial widths of 1.054 ± 0.010 and 0.965 ± 0.010 mm, and energy-closure widths of 12.19 ± 0.09 and 12.43 ± 0.10 MeV, respectively. These results demonstrate that signal events originating in the cryogenic liquid are reconstructed with vertex and energy resolutions comparable to those in the beam pipe. The radial resolution scale also establishes the feasibility of cleanly isolating liquid interactions from beam-pipe backgrounds. The 6.7 mm physical gap between the outer beam-pipe surface and the inner liquid boundary corresponds to $6.4\,\sigma_{68}$ of the beam-pipe vertex resolution.

4 Effective target densities and projected signal yields

4.1 Effective target densities

To compare the cryogenic targets with the existing beam pipe (BP), we define the effective areal number density encountered by an incident particle of species Y within $|\cos\theta| < 0.8$ as

$$\mathcal{T}_Y = \frac{\rho\,\langle l\rangle_Y}{M}\,N_A, \tag{7}$$

where ρ is the mass density, M is the molar mass of the scattering center (atomic H for free protons in LH_2; atomic D, providing one proton and one neutron, in LD_2), and N_A is Avogadro's number. We adopt $\rho = 0.0708\ \mathrm{g\cdot cm^{-3}}$ and $M = 1.008\ \mathrm{g\cdot mol^{-1}}$ for LH_2, and $\rho = 0.164\ \mathrm{g\cdot cm^{-3}}$ and $M = 2.014\ \mathrm{g\cdot mol^{-1}}$ for LD_2.

The effective path length $\langle l\rangle_Y$ is governed by the decay survival probability $S_Y(r,\theta)$ of Eq. (1). A particle emitted at polar angle θ traverses a radial interval $\mathrm{d}r$ along an oblique path element $\mathrm{d}r/\sin\theta$; given azimuthal symmetry, only the polar-angle distribution $f_Y(\cos\theta)$ of

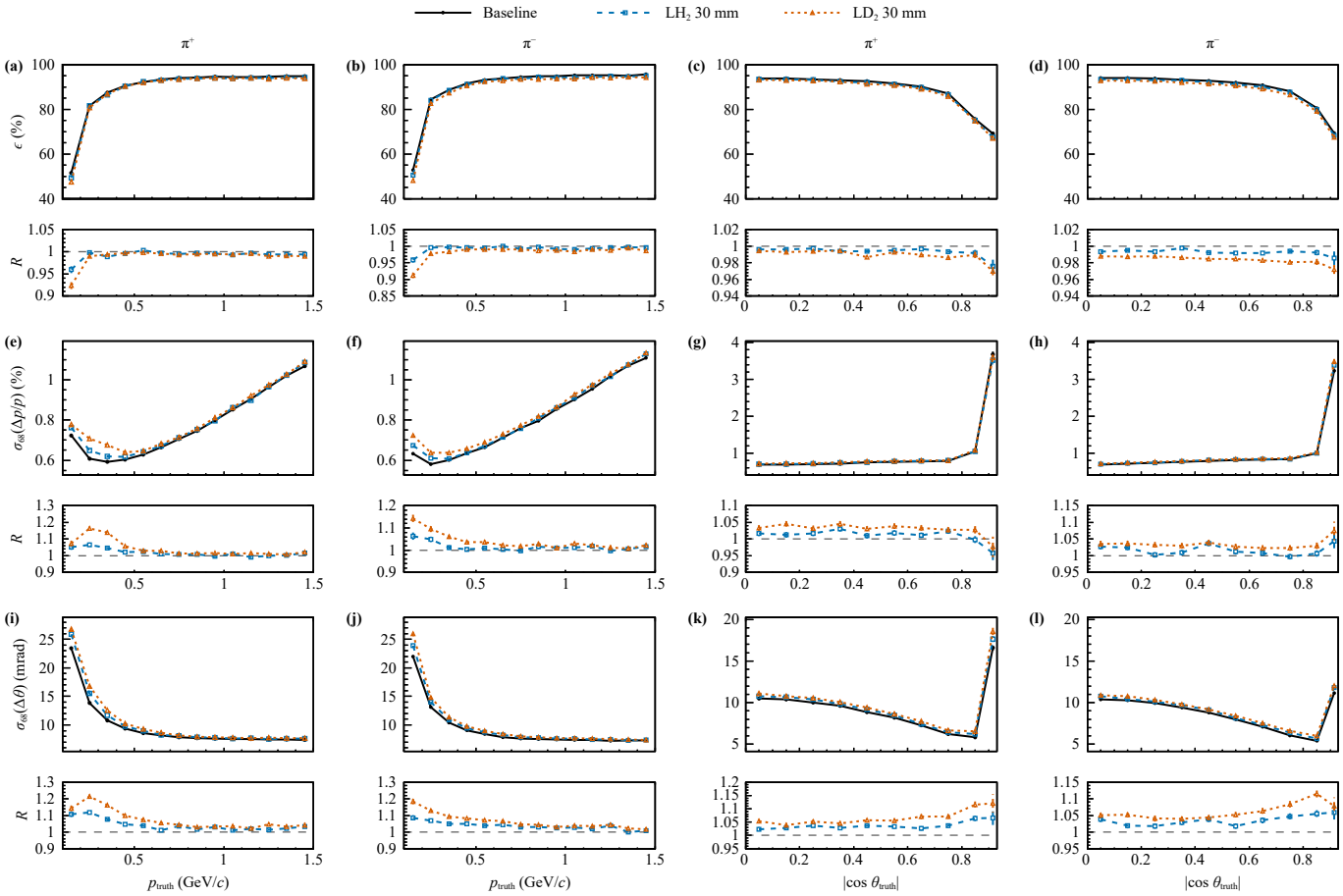


Fig. 5 Single-particle tracking performance for π^+ and π^-, using the same observables, layout, configurations, and axis conventions as in Fig. 3. The truth-momentum range spans 0.1–1.5 GeV/c.

Section 2.2 enters. For a cylindrical layer bounded by inner and outer radii $R_{\rm in}$ and $R_{\rm out}$, the mean path length of accepted particles is therefore

$$\langle l\rangle_Y = \frac{1}{A_Y}\int_{-0.8}^{0.8} f_Y(\cos\theta)\int_{R_{\rm in}}^{R_{\rm out}} \frac{S_Y(r,\theta)}{\sin\theta}\,\mathrm{d}r\,\mathrm{d}\cos\theta. \quad (8)$$

For hyperons, the inputs are those of Table 2. For antineutrons, which are stable on the scale of the detector ($S_{\bar n}=1$), Eq. (8) simplifies to $t\,\langle 1/\sin\theta\rangle$, where $t = R_{\rm out} - R_{\rm in}$ denotes the radial layer thickness. In this case, the average is evaluated over the 415 250 accepted PWA events that represent $f_{\bar n}$.

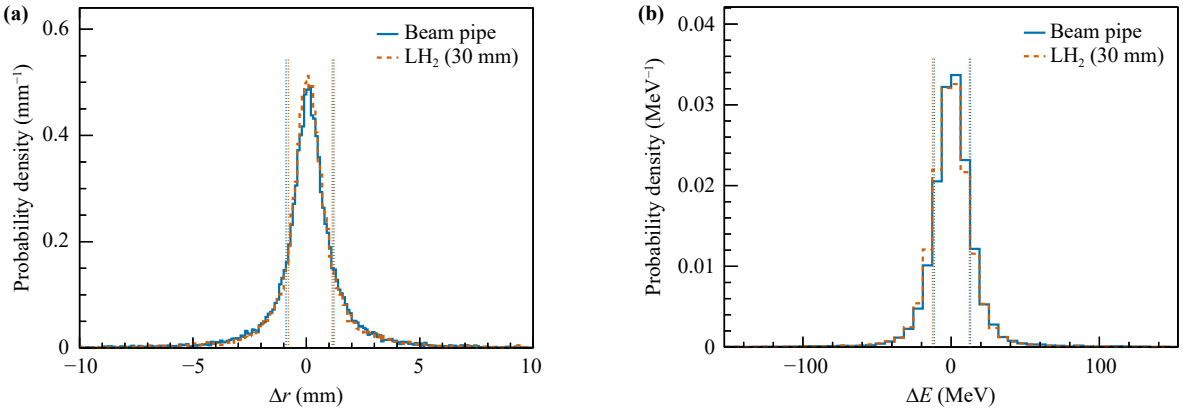


Fig. 6 Reconstruction performance for forced $\bar np \to 2\pi^+\pi^-$ annihilations for truth-matched signal tracks in the beam-pipe and 30 mm LH_2 configurations: **(a)** radial residual Δr of the common three-pion secondary vertex; **(b)** energy closure ΔE of the three-pion system relative to the tagged antineutron and a target proton at rest. Dashed lines mark the 16th and 84th percentiles of each full distribution.

Table 3 Angular acceptance A_Y, conditional boundary survival probabilities $S_Y(R_{\rm in/out})$, and mean path lengths within $|\cos\theta_Y| < 0.8$. Values for $\langle l\rangle_{\rm liquid}$ $(4.04 < r < 7.04$ cm) apply to both LH_2 and LD_2; the cooling oil spans $3.23 < r < 3.31$ cm. Hyperon uncertainties are propagated from Table 2; antineutron uncertainties are MC statistical only.

Species	A_Y	$S_Y(R_{\rm in})$	$S_Y(R_{\rm out})$	$\langle l\rangle_{\rm liquid}$ (cm)	$\langle l\rangle_{\rm oil}$ (cm)
Λ	0.76065 ± 0.00027	0.5360 ± 0.0013	0.3393 ± 0.0014	1.4857 ± 0.0048	0.05599 ± 0.00011
Σ^+	0.8587 ± 0.0010	0.10485 ± 0.00076	0.02058 ± 0.00025	0.1689 ± 0.0016	0.014175 ± 0.000084
Ξ^-	0.7529 ± 0.0010	0.2105 ± 0.0030	0.0682 ± 0.0016	0.4267 ± 0.0079	0.02586 ± 0.00030
Ξ^0	0.7579 ± 0.0011	0.419 ± 0.011	0.222 ± 0.010	1.066 ± 0.038	0.0457 ± 0.0010
Ω^-	0.7787 ± 0.0082	0.01861 ± 0.00098	0.001098 ± 0.000098	0.0200 ± 0.0013	0.00344 ± 0.00015
$\bar{n}$	0.8305 ± 0.0005	1	1	3.44675 ± 0.00078	0.091913 ± 0.000021

Applying Eq. (8) to both the liquid layer and the beam-pipe cooling oil $(3.23 < r < 3.31$ cm) yields the mean path lengths summarized in Table 3, with upstream material interactions neglected. Propagating the parameter uncertainties of Table 2 gives relative density uncertainties of 0.32%–6.35%, dominated by the hyperon lifetimes.

In the existing beam pipe (BP), free protons are present only in the 0.8 mm cooling-oil layer [37], so the comparison of the LH_2 target with this baseline is model-independent. For the bound nucleons in Be, C, and Au, previous BESIII analyses [33, 34, 36] adopted a surface-reaction model, in which a strongly absorbed projectile interacts mainly near the nuclear surface and the cross section per nucleus scales as $A^{2/3}$ rather than A. Each nucleus then contributes $A^{2/3}Z/A$ effective protons and $A^{2/3}(A-Z)/A$ effective neutrons, normalized such that a free nucleon counts as one. For antineutrons, this scaling reproduces the measured annihilation cross sections on C to Pb at 50–400 MeV/c within 2% [29]. For hyperons, comparable nuclear data are scarce, and the effective number of nucleons need not be the same for every reaction: it depends on how strongly the projectile is absorbed and on whether the reaction products rescatter or are captured in the nucleus. The few available estimates suggest deviations of tens of percent. An eikonal calculation for $^{12}C(\Xi^-, \Lambda\Lambda)X$ gave 3.0–4.1 effective protons, depending on the assumed cross section and Λ trapping probability [52], 14%–56% above the surface value of 2.62, and the BESIII $\Sigma^+ n$ and $\Xi^0 n$ analyses [33, 36] adopted about three effective neutrons for ^{9}Be, 25% above the surface value of 2.40. Such differences leave the order-of-magnitude comparisons in Tables 4 and 5, which use the surface values, unchanged, but they limit the precision of beam-pipe measurements in a way that more statistics cannot overcome. We take the 25% difference for ^{9}Be as the size of this uncertainty, assign it to the bound-nucleon densities of the beam pipe in Table 4, and list it in Table 6. The LD_2 target avoids it by replacing the composite Be, C, and Au nuclei with the weakly bound deuteron ($B = 2.22$ MeV), for which the nuclear corrections reduce to a few-body problem.

Combining these target definitions with the effective path lengths evaluated in Table 3, we obtain the effective areal number densities summarized in Table 4. The beam-pipe neutron and proton densities are the surface-model values, with the 25% nuclear-model uncertainty given as a separate error. Quantitatively, the 30 mm LH_2 target provides a dramatic enhancement in free-proton areal density, exceeding that of the cooling oil by factors of 7–22 for Λ, Σ^+, Ξ, and $\bar{n}$. This gain peaks at 21.7 for stable antineutrons and gradually decreases for shorter-lived hyperons (6.9 for Σ^+ and 3.4 for Ω^-) due to decay losses prior to reaching the liquid volume. For neutrons, by contrast, LD_2 yields 0.4–2.9 times the surface-weighted beam-pipe density. The primary merit of the LD_2 target is therefore qualitative rather than purely statistical: it provides a comparable effective

Table 4 Effective areal number densities $\mathcal{T}_Y$ (in units of 10^{22} cm^{-2}) for the beam pipe (BP) and the 30 mm liquid targets, for incident particles within $|\cos\theta_Y| < 0.8$. For the BP, the neutron (n) and total-proton (p) columns use the surface prescription described in the text, and the free-proton column (p_f) is the hydrogen in the cooling oil. The LH_2 column gives free protons; the LD_2 column counts one neutron or one proton per deuteron. The first error propagates the hyperon inputs, or the finite PWA statistics for $\bar{n}$. The BP n and p entries carry a second error, the 25% nuclear-model uncertainty of the effective number of bound nucleons (Section 4.1). Material and geometry uncertainties are not included.

Beam Y	BP (n)	BP (p)	BP (p_f)	LH_2 (p_f)	LD_2 (n/p)
Λ	$3.5447 \pm 0.0069 \pm 0.89$	$3.3294 \pm 0.0065 \pm 0.83$	0.40843 ± 0.00080	6.284 ± 0.020	7.286 ± 0.024
Σ^+	$0.9042 \pm 0.0053 \pm 0.23$	$0.8482 \pm 0.0050 \pm 0.21$	0.10340 ± 0.00061	0.7143 ± 0.0066	0.8281 ± 0.0076
Ξ^-	$1.644 \pm 0.019 \pm 0.41$	$1.543 \pm 0.018 \pm 0.39$	0.1886 ± 0.0022	1.805 ± 0.033	2.093 ± 0.039
Ξ^0	$2.898 \pm 0.064 \pm 0.72$	$2.721 \pm 0.060 \pm 0.68$	0.3335 ± 0.0074	4.51 ± 0.16	5.23 ± 0.19
Ω^-	$0.2215 \pm 0.0095 \pm 0.055$	$0.2074 \pm 0.0089 \pm 0.052$	0.0251 ± 0.0011	0.0844 ± 0.0054	0.0979 ± 0.0062
$\bar{n}$	$5.8030 \pm 0.0013 \pm 1.5$	$5.4533 \pm 0.0012 \pm 1.4$	0.67048 ± 0.00015	14.5792 ± 0.0033	16.9023 ± 0.0038

Table 5 Annual reference counts for the 30 mm liquid targets and 1.85×10^{10} J/ψ events ($G_{\rm parent}=1.834$); $N_{\rm rec}^{\rm proj}$ assumes unchanged efficiency. The density ratio $G_{\rm target}=\mathcal{T}_{Y,\rm liquid}/\mathcal{T}_{Y,\rm BP}$ uses the BP free-proton density for the free-proton channels, the total BP proton density for $\Lambda p\to\Sigma^+X$, and the BP neutron density for the neutron channels (Table 4). For $\Lambda p\to\Sigma^+X$ and the neutron channels, σ_N is a nucleon-level reference value inferred from Be, and only $N_{\rm prod}$ is given (Section 4.2). Published yields and cross sections are from Refs. [32–36]. The Λp and $\bar\Lambda p$ cross sections are those measured within $|\cos\theta^*|<0.9$ [35]. Errors on $N_{\rm prod}$ reflect cross-section statistical and systematic uncertainties; errors on $N_{\rm rec}^{\rm proj}$ propagate published BP statistical uncertainties only. The CW scenario illustrates an optional tenfold luminosity upgrade ($10N_{\rm rec}^{\rm proj}$).

Process	$G_{\rm target}$	σ_N (mb)	$N_{\rm prod}$ (10^3)	$N_{\rm BP}^{\rm pub}$	$N_{\rm rec}^{\rm proj}$	CW scenario
$\Lambda p_f\to\Lambda p$	15.39	$12.2\pm1.6\pm1.1$	$20.39\pm2.67\pm1.84$	60.9 ± 7.8	1719 ± 220	$\sim17{,}000$
$\bar\Lambda p_f\to\bar\Lambda p$	15.39	$17.5\pm2.1\pm1.6$	$29.25\pm3.51\pm2.67$	72.0 ± 8.5	2032 ± 240	$\sim20{,}000$
$\bar np_f\to2\pi^+\pi^-$	21.74	$2.7\pm0.3\pm0.3$	$12.82\pm1.42\pm1.42$	59.0 ± 7.7	2353 ± 307	$\sim24{,}000$
$\bar np_f\to2\pi^+\pi^-\pi^0$	21.74	$10.8\pm0.8\pm0.9$	$51.29\pm3.80\pm4.27$	182.0 ± 13.5	7259 ± 538	$\sim73{,}000$
$\bar np_f\to2\pi^+\pi^-2\pi^0$	21.74	$12.6\pm1.3\pm1.0$	$59.84\pm6.17\pm4.75$	97.7 ± 10.0	3897 ± 399	$\sim39{,}000$
$\Lambda p\to\Sigma^++X$	1.887	$19.3\pm2.4\pm1.8$	$32.26\pm4.01\pm3.01$	795 ± 101	–	–
$\Sigma^+n\to\Lambda p$	0.9158	$18.8\pm5.0\pm3.0$	$2.65\pm0.71\pm0.42$	77.6 ± 20.8	–	–
$\Sigma^+n\to\Sigma^0p$	0.9158	$12.4\pm4.0\pm2.9$	$1.75\pm0.57\pm0.40$	48.6 ± 15.9	–	–
$\Xi^0n\to\Xi^-p$	1.804	$9.19\pm2.20\pm1.87$	$7.88\pm1.89\pm1.61$	22.9 ± 5.5	–	–

neutron areal density while replacing heavy-nucleus medium effects with those of the few-body deuteron system.

4.2 Projected signal yields

To project the experimental sensitivity, we define two reaction counts for each channel. The first is the number of reactions produced in the target prior to tag and signal reconstruction:

$$N_{\rm prod}=N_{\rm parent}\,\mathcal{B}_{\rm tag}\,A_Y\,\mathcal{T}_Y\,\sigma_N, \tag{9}$$

where $N_{\rm parent}$ is the number of produced J/ψ or $\psi(3686)$ events, $\mathcal{B}_{\rm tag}$ is the production branching fraction (Table 2), and σ_N is the reaction cross section per target nucleon, treated as constant over the incident momentum range. Free-proton reactions use measured σ_{Yp} values. For $\Lambda p\to\Sigma^+X$ and the neutron reactions, σ_N is a nucleon-level reference value inferred from Be: the published proton-level value for $\Lambda p\to\Sigma^+X$, obtained with the surface factor 1.93 [34], and the Be cross sections measured by BESIII [33, 36] divided by the surface factor 2.40 for the neutron reactions.

The second count estimates the reconstructed signal yield by scaling the yield $N_{\rm BP}^{\rm pub}$ observed in the corresponding published beam-pipe (BP) analysis:

$$N_{\rm rec}^{\rm proj}=N_{\rm BP}^{\rm pub}\,G_{\rm parent}\,G_{\rm target},\qquad G_{\rm parent}=\frac{N_{\rm parent}}{N_{\rm parent}^{\rm BP}},\quad G_{\rm target}=\frac{\mathcal{T}_{Y,\rm liquid}}{\mathcal{T}_{Y,\rm BP}}. \tag{10}$$

When the published baseline measures the same reaction on the same kind of target nucleon, the cross section σ_N,

Table 6 Systematic uncertainties of the published BP cross-section measurements, grouped by their status with the 30 mm liquid target, and the sources added by the target. Sizes are relative uncertainties in percent, as published for Λp and $\bar\Lambda p$ elastic scattering [35], $\Lambda N\to\Sigma^+X$ [34], Σ^+n [36], Ξ^0n [33], and the three $\bar np$ final states [32]. Removed sources are those specific to the composite beam-pipe nuclei and material; for LD_2, the nuclear terms are replaced by the deuteron corrections listed among the new sources. The effective number of bound nucleons was not assigned an uncertainty in the published analyses; the value given here is the 25% difference between three and 2.40 effective ^{9}Be neutrons (Section 4.1). Retained sources are given as the quadrature sum of all published terms not listed as removed. The new sources have not been evaluated numerically.

Status	Source	Published size (%)
Removed	Nuclear cross-section ratio	Σ^+X 3.6; Σ^+n 7.3; Ξ^0n 7.2
	Effective number of bound nucleons	Σ^+X, Σ^+n, Ξ^0n ∼25 (this work)
	Fermi motion of bound neutrons	Σ^+n 6.5, 12.8; Ξ^0n 10.0
	Material of the cooling devices	Σ^+X 6.1
Retained	All other sources (in quadrature)	Λp, $\bar\Lambda p$ 9.1; $\bar np$ 7.5–8.4; Σ^+X 6.3; Σ^+n 12.7, 17.9; Ξ^0n 16.2
New	Interactions in BP and walls	–
	Liquid density and cell thickness	–
	Deuteron corrections (LD_2 only)	–

the tagging branching fraction $\mathcal{B}_{\rm tag}$, and the absolute reconstruction efficiencies cancel. This projection assumes comparable overall efficiencies between the liquid target and the beam pipe ($\bar{\epsilon}_{Y,\rm liquid} \approx \bar{\epsilon}_{Y,\rm BP}$). We keep this assumption for all channels: $\bar{n}p \to 2\pi^+\pi^-$ is the only channel simulated with the full event (Section 3.3), its efficiency ratio of 0.864 is moderate, and the selection, which was taken over from the beam-pipe analysis, can be optimized for the liquid target.

To establish a defensible annual benchmark, we assume ten months (300 calendar days) of dedicated run time at either the J/ψ or the $\psi(3686)$; the two samples below are alternative running scenarios, not a combined annual program. The projected parent event samples are extrapolated directly from the demonstrated daily luminosity rates of earlier resonance runs: $1200\,\mathrm{pb}^{-1}$ accumulated over 86 days at the J/ψ peak in 2019 (BESIII collaboration-meeting report, unpublished) and $3208.5\,\mathrm{pb}^{-1}$ over 126 days at the $\psi(3686)$ in 2021 [53]. Accounting for a factor of 1.3 gain in integrated luminosity enabled by top-up injection [54], the expected annual delivered luminosities are $5.44\,\mathrm{fb}^{-1}$ at the J/ψ and $9.93\,\mathrm{fb}^{-1}$ at the $\psi(3686)$. Using standard reference cross sections of 3400 nb and 640 nb [55], these translate to annual planning benchmarks of 1.85×10^{10} J/ψ and 6.36×10^{9} $\psi(3686)$ events. Because the published beam-pipe analyses utilized the historical dataset of $(1.0087\pm0.0044)\times10^{10}$ J/ψ events [56], $G_{\rm parent}=1.834$ across all J/ψ channels in Table 5.

The inputs $\mathcal{B}_{\rm tag}$, A_Y, and $\mathcal{T}_Y$ are listed in Tables 2, 3, and 4; Table 5 gives $G_{\rm target}$ for each channel together with the resulting projected counts. The total enhancement factor is the product $G_{\rm parent}G_{\rm target}$. The crab-waist (CW) column of Table 5 illustrates a hypothetical tenfold increase in annual exposure, as might be enabled by the crab-waist scheme [57, 58], and equals $10N_{\rm rec}^{\rm proj}$. Uncertainties quoted on $N_{\rm rec}^{\rm proj}$ propagate the 7%–13% statistical errors of the published BP measurements, while those on $N_{\rm prod}$ propagate cross-section uncertainties.

For the free-proton channels Λp, $\bar{\Lambda}p$, and $\bar{n}p$, the LH_2 target increases annual yields by factors of 28–40 over published BP statistics, reaching 1.7×10^3 to 7.3×10^3 reconstructed events per year. For $\Lambda p\to\Sigma^+X$ and the quasi-free neutron reactions, Table 5 lists only the raw interaction counts $N_{\rm prod}$: 3.2×10^4 per year for $\Lambda p\to\Sigma^+X$ with LH_2, and $(1.7\text{–}2.6)\times10^3$ for $\Sigma^+n\to\Lambda p$ and Σ^0p and 7.9×10^3 for $\Xi^0n\to\Xi^-p$ with LD_2. Reconstructed counts are not extrapolated because the published efficiencies do not transfer to these targets. For $\Lambda p\to\Sigma^+X$, Eq. (10) does not apply [34]: the published sample also includes interactions in the MDC inner wall, which are not counted in $\mathcal{T}_{Y,\rm BP}$. For the neutron reactions, the overall efficiency depends strongly on Fermi motion, spectator momentum acceptance, and final-state interactions, which are not simulated here.

Ω^- scattering is not included in the projections: only 1.86% of accepted Ω^- hyperons reach the liquid layer (Table 3). With 6.36×10^9 $\psi(3686)$ events, Eq. (9) gives $N_{\rm prod}\approx0.23\,(\sigma_{\Omega p}/\mathrm{mb})$ per year; for an assumed $\sigma_{\Omega p}=20$ mb and an overall tag and signal efficiency of 10%, this corresponds to about 0.5 reconstructed events per year, so Ω^-–nucleon scattering remains out of reach at BESIII.

4.3 Systematic uncertainties

The liquid target changes the systematic uncertainties of the BP analyses used above in three ways: it removes none of the published sources for the free-proton channels, removes the terms that arise from the composite beam-pipe material for the nuclear-inferred and neutron channels, and adds sources of its own.

For the free-proton channels, the BP measurements already select interactions on the oil hydrogen, so LH_2 removes no published source. The 9.1% systematic uncertainty of Λp and $\bar{\Lambda}p$ elastic scattering is dominated by tracking, PID, and branching-fraction terms, while the selection terms were already found to be negligible with a Barlow test [35]. The $\bar{n}p$ analyses, in contrast, assign 0.5%–4.5% terms to ±10% variations of the kinematic-fit, vertex-fit, scattering-position, and $P(p_{\rm oil})$ requirements and 0.2%–1.4% to the ΔE fit, which include statistical fluctuations of the 59–182 signal events, and 1.8%–2.6% to the intermediate ρ and ω states [32]. These terms, 5.2%–6.5% in quadrature, could decrease with the 40 times larger sample, through Barlow tests of the selection variations and a better-constrained description of the intermediate states, although a larger sample may also reveal deviations that are not significant at present. In the optimistic case that these terms become negligible, about 5.2%–5.6% from the other sources would remain.

For $\Lambda p\to\Sigma^+X$, the published per-proton cross section was obtained from the ^{9}Be measurement with a Be-to-proton cross-section ratio of 1.93 from a surface-reaction assumption, with no uncertainty assigned to this ratio (about 25% from the effective-nucleon comparison of Section 4.1), and includes a 3.6% term from an alternative nuclear scaling [34]; LH_2 removes both, as well as the 6.1% term from the material of the cooling devices. For Σ^+n and Ξ^0n, LD_2 removes the 7.2%–7.3% nuclear-ratio terms and the 6.5%–12.8% terms that the published analyses assign to simulating the neutron at rest [33, 36]; these are replaced by deuteron corrections that remain to be quantified. The retained terms, 12.7%–17.9% for Σ^+n and 16.2% for Ξ^0n, still limit these channels, but they largely reflect the small published samples rather than the target. For example, the largest single term of the $\Sigma^+n\to\Sigma^0p$ measurement, 14.3%, arises from simulating an isotropic angular distribution that a larger sample could measure [36].

Operating with an internal liquid target introduces

new systematic considerations across all channels. Interactions occurring in the beam pipe and the passive target layers now act as backgrounds, while tracking and particle-identification (PID) efficiencies must be recalibrated with data to account for the added material budget. Beam-pipe interactions can be cleanly separated from the liquid volume by reconstructed vertex radius, facilitated by the $6.4\,\sigma_{68}$ clearance demonstrated in Section 3.3, while residual backgrounds from the containment walls can be subtracted using dedicated empty-target runs normalized to the tagged incident flux. Regarding target normalization, uncertainties in the liquid density and the cold cell thickness replace those of the cooling-oil layer. The liquid density is governed by its operating temperature; a temperature stability of 0.01 K, as achieved by the MUSE target, corresponds to a temperature-induced density variation of only 0.02% [40]; the absolute density normalization of the proposed target remains to be evaluated. The cold cell thickness is subject to thermal contraction and pressure-induced deflection, which must be experimentally calibrated for this annular geometry. Thin-walled cryogenic targets in comparable experiments report thickness uncertainties of 1%–5% [59, 60]; adding only a 5% thickness uncertainty in quadrature to the published 9.1% systematic uncertainty of the benchmark Λp measurement would give 10.4%, before the other target-induced sources are included. A systematic breakdown across all channels is summarized in Table 6, categorizing sources into those removed, retained, or introduced by the liquid target, with unaffected terms combined in quadrature.

5 Conclusion and discussion

We have studied the feasibility of an internal LH_2 or LD_2 target between the beam pipe and the CGEM-IT at BESIII. The present beam-pipe measurements have two limitations: free protons exist only in the thin cooling-oil layer, which limits the statistics of free-proton scattering, and neutron scattering relies on neutrons bound in Be, C, and Au nuclei, which requires nuclear-model corrections. A pure hydrogen or deuterium target addresses both.

For the free-proton channels Λp, $\bar{\Lambda} p$, and $\bar{n}p$, a 30 mm LH_2 layer increases the effective free-proton areal density relative to the beam pipe by factors of 15.4 for the Λ and $\bar{\Lambda}$ beams and 21.7 for the $\bar{n}$ beam. Scaled from the published beam-pipe yields at unchanged efficiency, one year of running would give 28–40 times the published samples, with statistical errors of 1.2%–2.4%, well below the published systematic uncertainties of 7.5%–9.1%. The gain for these channels is therefore statistical and benefits mainly differential measurements. For $\Lambda p \to \Sigma^+ X$, whose published cross section was inferred from Be, LH_2 removes the nuclear-scaling (3.6%) and cooling-material (6.1%) terms and the uncertainty of the Be-to-proton ratio. For $\Sigma^+ n$ and $\Xi^0 n$, an LD_2 target, with neutron areal densities 0.92 and 1.80 times those of the beam pipe, replaces the composite beam-pipe nuclei by the deuteron. This removes the nuclear cross-section-ratio terms (7.2%–7.3%) and the bound-neutron Fermi-motion terms (6.5%–12.8%) of the published measurements, as well as the ambiguity of about 25% in the effective number of Be neutrons, in exchange for deuteron corrections that remain to be quantified. For the Ω^-, decays before the target leave about 0.5 reconstructed events per year for an assumed 20 mb cross section and 10% efficiency, and about five even with the tenfold exposure of the illustrative crab-waist scenario, so $\Omega^- N$ scattering remains highly challenging at BESIII. None of these estimates includes channel-dependent efficiencies or backgrounds.

In the single-particle simulations, the target affects tracking mainly below 0.5 GeV/c. Above 0.5 GeV/c, the efficiencies of protons, kaons, and pions stay within 1.6 percentage points of the baseline, while the antiproton efficiency is lower by up to 2.2 (LH_2) and 4.9 (LD_2) points. In the signal-only full-event simulation of $\bar{n}p \to 2\pi^+\pi^-$, LH_2 lowers the conditional selection efficiency by 14% relative to the beam pipe, and the vertex and energy-closure resolutions of liquid-target events, $\sigma_{68} \approx 1.0$ mm and 12 MeV, are comparable to those of beam-pipe events. The 6.7 mm gap between the beam pipe and the liquid corresponds to 6.4 times the beam-pipe radial resolution, so interactions in the two can be separated by vertex radius.

The engineering of the target, including the heat load and cooling, installation clearances, compatibility with the beam vacuum and the CGEM-IT, and hydrogen safety, remains to be studied. If cryogenic operation proves impractical, room-temperature hydrogen- or deuterium-rich materials such as $(CH_2)_n$, $(CD_2)_n$, LiH, or D_2O could serve as alternatives, at the cost of additional nuclei in the target. Apart from the antineutron, the beams considered here come from two-body decays at fixed momenta; hyperons from multi-body J/ψ and $\psi(3686)$ decays could extend the measurements over a continuous momentum range, and their yields and backgrounds remain to be evaluated. Overall, an internal hydrogen or deuterium target is a promising concept for higher-statistics and less model-dependent YN and $\bar{n}N$ scattering measurements at BESIII and, with larger resonance samples, at future facilities such as STCF [61] and SCTF [62]; it requires further engineering and channel-level validation.

Declarations The authors declare that they have no competing interests and there are no conflicts.

Acknowledgements This work was supported in part by the National Natural Science Foundation of China under contract No.

12361141819 and the Program of Science and Technology Development Plan of Jilin Province of China under contract No. 20230101021JC.

References

1. E. Epelbaum, H. W. Hammer, and U. G. Meißner, Modern theory of nuclear forces, *Rev. Mod. Phys.* 81(4), 1773 (2009)
2. R. Machleidt and D. R. Entem, Chiral effective field theory and nuclear forces, *Phys. Rep.* 503(1), 1 (2011)
3. S. K. Bogner, R. J. Furnstahl, and A. Schwenk, From low-momentum interactions to nuclear structure, *Prog. Part. Nucl. Phys.* 65(1), 94 (2010)
4. E. Klempt, F. Bradamante, A. Martin, and J. M. Richard, Antinucleon-nucleon interaction at low energy: scattering and protonium, *Phys. Rep.* 368(2–3), 119 (2002)
5. T. Bressani and A. Filippi, Antineutron physics, *Phys. Rep.* 383(4), 213 (2003)
6. A. Gal, E. V. Hungerford, and D. J. Millener, Strangeness in nuclear physics, *Rev. Mod. Phys.* 88(3), 035004 (2016)
7. L. Tolos and L. Fabbietti, Strangeness in nuclei and neutron stars, *Prog. Part. Nucl. Phys.* 112, 103770 (2020)
8. P. B. Demorest, T. Pennucci, S. M. Ransom, M. S. E. Roberts, and J. W. T. Hessels, A two-solar-mass neutron star measured using Shapiro delay, *Nature* 467(7319), 1081 (2010)
9. J. Antoniadis, P. C. C. Freire, N. Wex, T. M. Tauris, R. S. Lynch, et al., A massive pulsar in a compact relativistic binary, *Science* 340(6131), 448 (2013)
10. D. Lonardoni, A. Lovato, S. Gandolfi, and F. Pederiva, Hyperon puzzle: Hints from quantum Monte Carlo calculations, *Phys. Rev. Lett.* 114(9), 092301 (2015)
11. D. Gerstung, N. Kaiser, and W. Weise, Hyperon–nucleon three-body forces and strangeness in neutron stars, *Eur. Phys. J. A* 56(6), 175 (2020)
12. G. Alexander, U. Karshon, A. Shapira, G. Yekutieli, R. Engelmann, H. Filthuth, and W. Lughofer, Study of the Λ–N system in low-energy Λ–p elastic scattering, *Phys. Rev.* 173(5), 1452 (1968)
13. B. Sechi-Zorn, B. Kehoe, J. Twitty, and R. A. Burnstein, Low-energy Λ-proton elastic scattering, *Phys. Rev.* 175(5), 1735 (1968)
14. J. A. Kadyk, G. Alexander, J. H. Chan, P. Gaposchkin, and G. H. Trilling, Λp interactions in momentum range 300 to 1500 MeV/c, *Nucl. Phys. B* 27(1), 13 (1971)
15. F. Eisele, H. Filthuth, W. Föhlisch, V. Hepp, and G. Zech, Elastic $\Sigma^{\pm}$p scattering at low energies, *Phys. Lett. B* 37(2), 204 (1971)
16. J. M. Hauptman, J. A. Kadyk, and G. H. Trilling, Experimental study of Λp and Ξ^0p interactions in the range 1–10 GeV/c, *Nucl. Phys. B* 125(1), 29 (1977)
17. K. Miwa, et al. [J-PARC E40 Collaboration], Precise measurement of differential cross sections of the $\Sigma^- p \to \Lambda n$ reaction in momentum range 470–650 MeV/c, *Phys. Rev. Lett.* 128(7), 072501 (2022)
18. K. Miwa, et al. [J-PARC E40 Collaboration], Measurement of the differential cross sections of the $\Sigma^- p$ elastic scattering in momentum range 470 to 850 MeV/c, *Phys. Rev. C* 104(4), 045204 (2021)
19. T. Nanamura, et al. [J-PARC E40 Collaboration], Measurement of differential cross sections for $\Sigma^+ p$ elastic scattering in the momentum range 0.44–0.80 GeV/c, *Prog. Theor. Exp. Phys.* 2022(9), 093D01 (2022)
20. J. Rowley, et al. [CLAS Collaboration], Improved Λp elastic scattering cross sections between 0.9 and 2.0 GeV/c as a main ingredient of the neutron star equation of state, *Phys. Rev. Lett.* 127(27), 272303 (2021)
21. J. Haidenbauer, U. G. Meißner, A. Nogga, and H. Le, Hyperon–nucleon interaction in chiral effective field theory at next-to-next-to-leading order, *Eur. Phys. J. A* 59(3), 63 (2023)
22. J. Song, Z. W. Liu, K. W. Li, and L. S. Geng, Test of the hyperon-nucleon interaction within leading order covariant chiral effective field theory, *Phys. Rev. C* 105(3), 035203 (2022)
23. K. Sasaki, et al. [HAL QCD Collaboration], ΛΛ and NΞ interactions from lattice QCD near the physical point, *Nucl. Phys. A* 998, 121737 (2020)
24. A. Bertin, et al. [OBELIX Collaboration], Study of the $f_0(1500)/f_2(1565)$ production in the exclusive annihilation $\bar{n}p\pi^+\pi^+\pi^-$ in flight, *Phys. Rev. D* 57(1), 55 (1998)
25. V. G. Ableev, et al. [OBELIX Collaboration], ϕ and ω meson production in $\bar{n}p$ annihilation and the OZI rule, *Phys. Lett. B* 334(1–2), 237 (1994)
26. T. Armstrong, et al. [BNL-E-0767 Collaboration], Measurement of antineutron-proton total and annihilation cross sections from 100 to 500 MeV/c, *Phys. Rev. D* 36(3), 659 (1987)
27. M. Agnello, E. Botta, T. Bressani, D. Calvo, A. Feliciello, et al., The antineutron beam at OBELIX, *Nucl. Instrum. Methods Phys. Res. Sect. A* 399(1), 11 (1997)
28. F. Iazzi, et al. [OBELIX Collaboration], Antineutron-proton total cross section from 50 to 400 MeV/c, *Phys. Lett. B* 475(3–4), 378 (2000)
29. M. Astrua, E. Botta, T. Bressani, D. Calvo, C. Casalegno, A. Feliciello, A. Filippi, S. Marcello, M. Agnello, and F. Iazzi, Antineutron-nucleus annihilation cross sections below 400 MeV/c, *Nucl. Phys. A* 697(1–2), 209 (2002)
30. C. Z. Yuan and M. Karliner, Cornucopia of antineutrons and hyperons from a super J/ψ factory for next-generation nuclear and particle physics high-precision experiments, *Phys. Rev. Lett.* 127(1), 012003 (2021)
31. J. P. Dai, H. B. Li, H. Miao, and J. Y. Zhang, Prospects to study hyperon-nucleon interactions at BESIII, *Chin. Phys. C* 48(7), 073003 (2024)
32. M. Ablikim, et al. [BESIII Collaboration], Study of the reactions $\bar{n}p \to 2\pi^+\pi^-$, $2\pi^+\pi^-\pi^0$, and $2\pi^+\pi^-2\pi^0$ using $J/\psi \to p\pi^-\bar{n}$, *Phys. Rev. Lett.* 137(3), 031902 (2026)
33. M. Ablikim, et al. [BESIII Collaboration], First study of reaction $\Xi^0 n \to \Xi^- p$ using Ξ^0-nucleus scattering at an electron-positron collider, *Phys. Rev. Lett.* 130(25), 251902 (2023)
34. M. Ablikim, et al. [BESIII Collaboration], First measurement of ΛN inelastic scattering with Λ from $e^+e^- \to J/\psi \to \Lambda\bar{\Lambda}$, *Phys. Rev. C* 109(5), L052201 (2024)
35. M. Ablikim, et al. [BESIII Collaboration], First study of

antihyperon-nucleon scattering $\bar{\Lambda}p \to \bar{\Lambda}p$ and measurement of $\Lambda p \to \Lambda p$ cross section, *Phys. Rev. Lett.* 132(23), 231902 (2024)
36. M. Ablikim, et al. [BESIII Collaboration], First measurement of $\Sigma^+ n \to \Lambda p$ and $\Sigma^+ n \to \Sigma^0 p$ cross sections via Σ^+-nucleus scattering at an electron-positron collider, *Phys. Rev. C* 113(3), L032201 (2026)
37. M. Ablikim, et al. [BESIII Collaboration], Design and construction of the BESIII detector, *Nucl. Instrum. Methods Phys. Res. Sect. A: Accel., Spectrometers, Detectors Assoc. Equip.* 614(3), 345 (2010)
38. C. H. Yu, Z. Duan, S. D. Gu, Y. Y. Guo, X. Y. Huang, et al., BEPCII performance and beam dynamics studies on luminosity. Proceedings of the 7th International Particle Accelerator Conference, Busan, 2016, pp 1014–1018
39. I. Balossino, F. Cossio, R. Farinelli, and L. Lavezzi, The CGEM-IT: An upgrade for the BESIII experiment, *Symmetry* 14(5), 905 (2022)
40. P. Roy, S. Corsett, M. Dimond, M. Kim, L. Le Pottier, et al., A liquid hydrogen target for the MUSE experiment at PSI, *Nucl. Instrum. Methods Phys. Res. Sect. A.* 949, 162874 (2020)
41. G. Fäldt and A. Kupsc, Hadronic structure functions in the $e^+e^- \to \bar{\Lambda}\Lambda$ reaction, *Phys. Lett. B* 772, 16 (2017)
42. E. Perotti, G. Fäldt, A. Kupsc, S. Leupold, and J. J. Song, Polarization observables in e^+e^- annihilation to a baryon–antibaryon pair, *Phys. Rev. D* 99(5), 056008 (2019)
43. M. Ablikim, et al. [BESIII Collaboration], Precise measurements of decay parameters and *CP* asymmetry with entangled Λ–$\bar{\Lambda}$ pairs, *Phys. Rev. Lett.* 129(13), 131801 (2022)
44. M. Ablikim, et al. [BESIII Collaboration], Probing CP symmetry and weak phases with entangled double-strange baryons, *Nature* 606(7912), 64 (2022)
45. M. Ablikim, et al. [BESIII Collaboration], Σ^+ and $\bar{\Sigma}^-$ polarization in the J/ψ and $\psi(3686)$ decays, *Phys. Rev. Lett.* 125(5), 052004 (2020)
46. M. Ablikim, et al. [BESIII Collaboration], Tests of *CP* symmetry in entangled Ξ^0–$\bar{\Xi}^0$ pairs, *Phys. Rev. D* 108(3), L031106 (2023)
47. M. Ablikim, et al. [BESIII Collaboration], Model-independent determination of the spin of the Ω^- and its polarization alignment in $\psi(3686) \to \Omega^-\bar{\Omega}^+$, *Phys. Rev. Lett.* 126(9), 092002 (2021)
48. S. Navas, et al. [Particle Data Group Collaboration], Review of particle physics, *Phys. Rev. D* 110(3), 030001 (2024)
49. S. C. Yuan, L. L. Wang, and W. D. Li, An approach to study interactions of antineutrons with CsI at a J/ψ factory, *Radiat. Detect. Technol. Methods* 8(3), 1405 (2024)
50. E. B. Wilson, Probable inference, the law of succession, and statistical inference, *J. Am. Stat. Assoc.* 22(158), 209 (1927)
51. B. Efron, Bootstrap methods: another look at the jackknife, *Ann. Statist.* 7(1), 1 (1979)
52. J. K. Ahn, S. Aoki, K. S. Chung, M. S. Chung, H. En'yo, et al., Measurement of the $\Xi^- p$ scattering cross sections at low energy, *Phys. Lett. B* 633(2–3), 214 (2006)
53. M. Ablikim, et al. [BESIII Collaboration], Determination of the number of $\psi(3686)$ events taken at BESIII, *Chin. Phys. C* 48(9), 093001 (2024)
54. M. Ablikim, et al. [BESIII Collaboration], Future physics programme of BESIII, *Chin. Phys. C* 44(4), 040001 (2020)
55. H. B. Li, Prospects of probing rare and forbidden processes at BES-III (2006)
56. M. Ablikim, et al. [BESIII Collaboration], Number of J/ψ events at BESIII, *Chin. Phys. C* 46(7), 074001 (2022)
57. M. Zobov [DAΦNE Team], Crab Waist collision scheme: A novel approach for particle colliders, *J. Phys. Conf. Ser.* 747, 012090 (2016)
58. A. Bogomyagkov and E. Levichev, Possibilities of crab waist (2016)
59. V. Klimenko, et al. [CLAS Collaboration], Inclusive electron scattering in the resonance region off a hydrogen target with CLAS12, *Phys. Rev. C* 112(2), 025201 (2025)
60. R. Ramazani-Sharifabadi, A. Ramazani-Moghaddam-Arani, H. R. Amir-Ahmadi, C. D. Bailey, A. Deltuva, et al., Precision measurements of differential cross sections and analyzing powers in elastic deuteron-deuteron scattering at 65 MeV/nucleon, *Eur. Phys. J. A* 57(4), 119 (2021)
61. M. Achasov, et al. [STCF Collaboration], STCF conceptual design report (Volume 1): Physics & detector, *Front. Phys. (Beijing)* 19(1), 14701 (2024)
62. A. E. Bondar, et al. [Super Charm-Tau Factory Collaboration], Project of a super charm-tau factory at the Budker Institute of Nuclear Physics in Novosibirsk, *Phys. Atom. Nucl.* 76(9), 1072 (2013)